PERGAMON

International Journal of Heat and Mass Transfer 42 (1999) 287–301

International Journal of HEAT and MASS TRANSFER

# Critical heat flux of water subcooled flow in one-side heated swirl tubes

J. Boscary[a,*,1], J. Fabre[a], J. Schlosser[b]

[a] *Institut de Mécanique des Fluides, Allée du Professeur Camille Soula, 31400 Toulouse, France*
[b] *Association Euratom CEA-Cadarache, Département de Recherche sur la Fusion Contrôlée, 13108 Saint Paul-Lez-Durance, France*

Received 26 May 1997; in final form 9 March 1998

**Abstract**

This paper reports an investigation of the critical heat flux (CHF) in the subcooled flow boiling regime. Hardened copper tube is heated on one side of its external rectangular section like for fusion reactor plasma facing components. It is cooled by a subcooled water flowing in a circular channel equipped with an inserted twisted tape. During experiments, CHF is detected by means of an infrared camera picture. Experimental results corresponding to various thermal hydraulic conditions are reasonably well predicted by a correlation deduced from the sublayer dryout model proposed by Celata et al. This new correlation also applies to classical situations of parallel flow with axisymmetrical heating. 

**Nomenclature**

$Bo = \Phi/(\rho_L U i_{fg})$ boiling number [dimensionless]
$C_P$ specific heat at constant pressure [J kg$^1$ K$^{-1}$]
$D$ channel diameter [m]
$Dh$ equivalent hydraulic diameter [m]
$f$ friction factor [dimensionless]
$F$ peaking factor [dimensionless]
$G$ mass flux [kg m$^{-2}$ s$^{-1}$]
$i$ enthalpy [J kg$^{-1}$]
$i_{fg}$ latent heat of vaporization [J kg$^{-1}$]
$L$ length [m]
$P$ pressure [MPa]
$Pr$ Prandtl number [dimensionless]
$Pr_t$ turbulent Prandtl number [dimensionless]
$Re = UD/v_L$ Reynolds number [dimensionless]
$S$ section [m$^2$]
$St = \Phi_w/[GC_P(T_w - T_{out})]$ Stanton number [dimensionless]
$t$ minimum thickness [m]
$T$ temperature [°C]
$u_*$ friction velocity [m s$^{-1}$]
$U$ velocity [m s$^{-1}$]
$w$ width [m]
$We = \rho_L U_L^2 D/\sigma$ Weber number [dimensionless]
$x = [C_P(T - T_{sat})]/i_{fg}$ enthalpic mass quality [dimensionless]
$y$ distance from the heated wall [m].

*Greek symbols*
$\delta$ tape thickness [m]
$\theta_*$ friction temperature
$\kappa$ Karman constant
$v$ cinematic viscosity [m$^2$ s$^{-1}$]
$\rho$ density [kg m$^{-3}$]
$\sigma$ surface tension [N m$^{-1}$]
$\Phi$ heat flux [W m$^{-2}$]
$\omega$ twist ratio.

*Subscripts*
b blanket
c critical
H heated
H1 one-side heated
i incident
in inlet
L liquid
out outlet
onb onset of nucleate boiling

* Corresponding author
[1] Present address: JAERI, 801-1 Naka-machi, Naka-gun, Ibaraki-ken, 311-01 Japan.

0017–9310/98/$—see front matter 
PII: S0017–9310(98)00108–2

sat saturation
sub subcooled
sw swirl
V vapour
w wall
+ dimensionless quantity.

## 1. Introduction

For tokamaks and also for the next generation machine of thermonuclear fusion, some components facing to plasma [1–3] may be submitted to high heat fluxes of several tens of $MW/m^2$ and requires cooling with pressurized subcooled water system. To design these components, it is of major importance to predict accurately the Critical Heat Flux (CHF) vs. the thermal hydraulic conditions.

Boiling CHF in water subcooled flow has been extensively studied for PWR operating conditions [4, 5] i.e. for an order of magnitude lower than fusion reactors. The first approach was to extend to high fluxes the CHF correlations developed for PWR thermal hydraulic conditions. So far, the Tong's correlation [6] is extensively used with specific modifications by laboratories working on cooling of high heat flux components for fusion application [7–12]. Recently, Celata [14, 15] proposed a new CHF model for the subcooled boiling regime based on the liquid sublayer dryout mechanism. This model which was originally developed for vertical upflow of water in uniform heated tubes has been checked here against thermal hydraulic conditions of fusion reactors with one side heating and high heat flux.

The first part of this paper describes the experimental study of different test sections installed in a vacuum chamber and heated by means of an electron beam gun. The influence of thermal hydraulic conditions on CHF, detected by the infrared visualisation of the heated surface, is analysed. The second part deals with CHF modelling. It is shown that Celata's model may be considerably simplified. This simplification that applies for original Celata's conditions of uniformly heated tubes is also extended to one-side heated tubes based on the present experimental data.

## 2. Experiments

### 2.1. Experimental facility

The experimental facility consists of a test section of 400 mm long, made of Glidcop Al-25 ($Cu–Al_2O_3$) which is a dispersion strengthened copper alloy (Fig. 1). The cross-section of this tube is circular inside and rectangular outside.

One of the external faces of this tube is submitted to a high thermal flux. This flux is obtained in the high thermal flux station FE 200 [16] which was brought into service in 1991 for testing plasma facing components. The heat flux is produced by an electron gun whose beam sweeps the exposed side of the test section installed in a vacuum chamber. The maximum gun power is 200 kW. The beam diameter is about 2 mm, i.e. 90% of the gun power falls within a 2 mm circle. A computer control system allows an accurate adjustment of the beam sweeping onto the heated zone. In the spanwise direction the flux is uniform while in the streamwise direction, it can be varied by controlling the sweeping velocity. To ensure that the heat

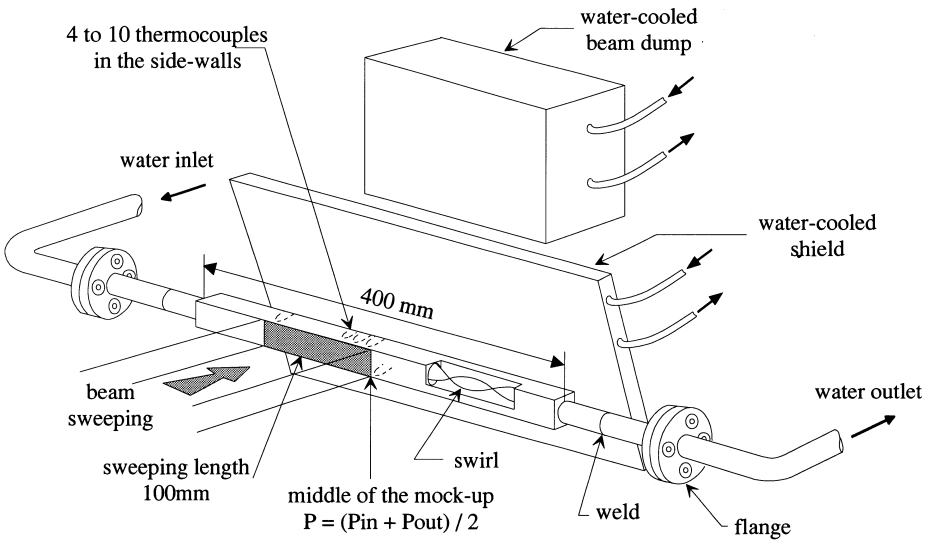


Fig. 1. Experimental facility.

flux is uniform in the spanwise direction, the sweeping width is 4 mm larger than the test section. To absorb these extra electrons, a water-cooled thermal shield is placed behind the test section. This shield is also useful to protect the opposite side of the test section against the reflected electrons. In the present study a uniform flux in both spanwise and streamwise directions was used.

The test section is cooled by subcooled water, flowing inside the circular section equipped with a stainless steel twisted tape acting as a turbulence promoter. This tape is held in position by weldings of its extremities on the stainless part of the test section. Water is supplied by a pressurised loop designed for removing a maximum power of 300 kW in steady state conditions. The loop is completely managed through an automaton by a remote control-command unit. Water is chemically treated by deoxygenation in order to avoid any corrosion problem. The maximum flow rate is 2 kg $s^{-1}$. The water pressure and the inlet temperature can be adjusted within the ranges 0.2–3.9 MPa and 30–230°C, respectively. The loop is equipped with pressure gauges, flow meters and temperature measurement devices.

The test sections are instrumented with four to ten brazed wall thermocouples. Four thermocouples are located near the heated surface and the others at different depths from the surface. These thermocouples are connected to the data acquisition system and displayed in real-time onto a screen to detect sudden temperature increase due to CHF and thus to protect the test section against burn-out.

The heated surface of the test section is observed by means of:

—A CCD colour camera and an infrared camera. The video-displayed images are tape recorded. The infrared images are processed by an Inframetrics™ software.
—Two optical laser-controlled pyrometers having different scales (0–800°C; 800–2000°C). The surface covered by a pyrometer is about 1 $cm^2$. The evolution of the surface temperature is displayed onto a screen to detect sudden temperature increases.

CHF is mainly detected by the infrared camera. This camera was calibrated up to 1500°C using a black body. The Inframetrics™ software takes into account the Glidcop emissivity and the transmission of the optical system between the test section and the camera. The transmission coefficient is found experimentally by using a black body. The determination of the emissivity coefficient of copper alloys is very tricky because its value greatly depends on the surface conditions. Therefore, the surface of the test section was previously sanded in order to reduce this sensitivity. The emissivity is then measured using a little block of the same material, thermally isolated from its metallic support and insulated by the electron beam to get a high temperature in steady state conditions (800°C during 30 s). Simultaneous temperature measurements from a thermocouple introduced inside the block and from the infrared camera focused on its surface are made. The emissivity is then adjusted so as to recover, from the software, the same temperature as the thermocouple. By doing so, rather realistic measurements of the surface temperature were obtained during the tests.

### 2.2. Experimental procedure

The test section is installed on a moving frame, connected to the water loop by flexible pipes and horizontally positioned into the vacuum chamber. For each test, the thermal hydraulic conditions (inlet temperature, inlet pressure, mass flow rate) and parameters that control the electron beam sweeping are selected. In the present experiments, the length of the heated zone was about 100 mm, its end corresponding to the middle of the test section (see Fig. 1).

Each test is performed by increasing the gun power step by step up to the detection of CHF. Each step consists of a cyclic process during which the beam alternatively sweeps the test section and the dump block for 80 and 5 s, respectively. The gun power is increased when the beam is pointed towards the dump block. This procedure allows several levels of power to be performed during the same test and provides enough time to determine the next power step.

CHF is mainly detected from infrared camera as follows (Fig. 2). Thermal hydraulic conditions are: $L_H = 100$ mm, $w_H = 24$ mm, $D = 18$ mm, $G = 8000$ kg $m^{-2} s^{-1}$, $P_{out} = 3.5$ MPa and $T_{in} = 49$°C. A picture of the surface temperature taken during non CHF situation (Fig. 2(a)) shows two hot zones, almost symmetrical with respect to the longitudinal axis of the test section: since the tube thickness is smaller near this axis, the thermal resistance is smaller and so is the surface temperature. When CHF occurs the two hot zones spread and join in the middle of the test section at the end of the heated surface (Fig. 2(b)). When a hot spot is detected, CHF is considered to start and heating is stopped in order to spare the mock-up. In few tests, heating was not stopped after that the hot spot detected: they showed that burn-out, leading to the wall destruction, occurred about one second after the detection of CHF. When CHF is approached, the CCD camera gives another qualitative information during the test: the colour picture shows that the surface of the heated region presents a melted and/or eroded appearance.

CHF can also be detected from the surface temperature measured by the two pyrometers and from the temperature inside the material measured by thermocouples. When one of these temperatures rises over some given value, the test can be stopped. But, this detection method is not always reliable because the temperature sensors are not necessarily located close to the small area where physical burn-out occurs.

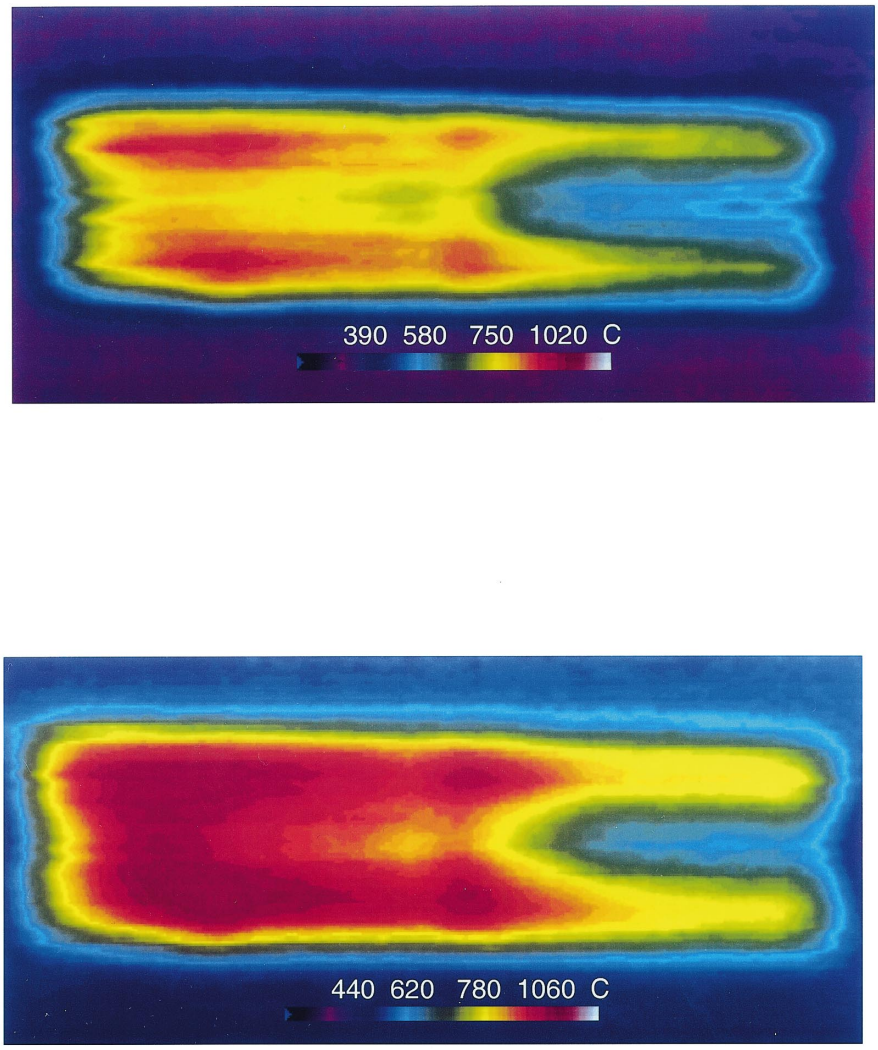


Fig. 2. Infrared pictures of the heated surface (inlet corresponds to the right of the picture): (a) during non CHF situation; (b) during CHF situation.

The test parameters, i.e. the beam parameters, the thermal hydraulic conditions and the local temperatures are continuously monitored, recorded and processed with a data acquisition frequency of 10 Hz.

### 2.3. Experimental results

Four mock-ups with a geometry shown in Fig. 3, were tested. They correspond to different values of the tube inside diameter, $D$, the width of the outside cross section, $w$ and the minimum thickness of the wall between the heated surface and the circular channel, $t$ (see Table 1). The cooling channel was drilled in the centre of the mock-up. The insert was made of stainless steel tape 0.8 mm thick. It was twisted so that the number of inner diameters for a twist of 180° was always equal to two.

A wide range of thermal hydraulic conditions defined by the inlet temperature $T_{in}$, the mass flux, $G$, the pressure at the end of the heated section, $P_{out}$ was explored. These conditions correspond to $T_{in} = 50$, 100, 150, 170°C, $G = 5$, 10, 12, 15 Mg m$^{-2}$ s$^{-1}$, $P_{out} = 1.3$, 2.4, 3.5 MPa. A database of 75 CHF conditions, among which 47 are given in Table 2, was obtained. For each test leading to CHF occurrence, the local temperatures at the surface and inside the material were recorded for at least 10 different steps of beam power. Consequently, about 750 sets of experimental data are available for understanding heat transfer in such geometries.

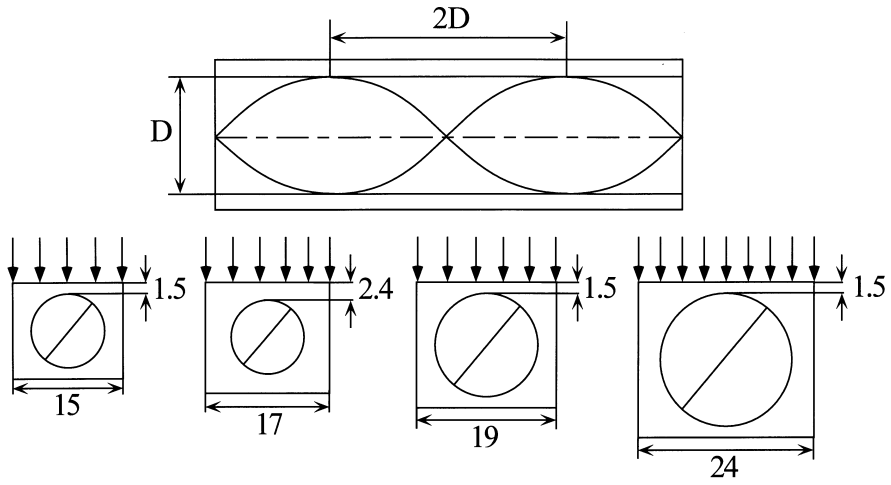


Fig. 3. Geometrical parameters of mock-ups.

Table 1
Dimensions of mock-ups

| Geometry No. | $D$ (mm) | $w$ (mm) | $t$ (mm) |
|---|---|---|---|
| 1 | 10 | 15 | 1.5 |
| 2 | 10 | 17 | 2.4 |
| 3 | 14 | 19 | 1.5 |
| 4 | 18 | 24 | 1.5 |

If the fluxes radiated by the non heated surfaces is neglected, the incident CHF, $\Phi_i$, is given by:

$$\Phi_i = \frac{GS(i_{out} - i_{in})}{L_H w_H} \quad (1)$$

where $S$ is the section of passage of the fluid, $L_H$, the heated length, $w_H$, the heated width, $i_{in}$ and $i_{out}$, the inlet and outlet enthalpies. These enthalpies are determined from inlet and outlet bulk temperature $T_{in}$ and $T_{out}$, measured by two sets of two platinum resistance probes, located at about 1 m upstream and downstream from the heated section. With this arrangement, the vapour generated at the outlet of the heated section is expected to be condensed in the subcooled liquid core, at the location where $T_{out}$ is measured.

The effect of the experimental thermal hydraulic parameters on the incident CHF are reported in Figs 4–6 for the geometry No. 3 (see Table 1). In Fig. 4, the incident CHF $\Phi_i$ is plotted vs. the mass flux $G$, for different subcoolings at the outlet. As expected the incident CHF is an increasing function of the mass flux within the investigated range. From a design point of view, it turns out that increasing the mass flow rate allows to increase the incident heat flux. However, the pressure drop increases too.

The influence of subcooling is illustrated in Fig. 5 where the incident CHF is plotted vs. the outlet subcooling for different mass fluxes. It appears that the incident CHF increases almost linearly with the subcooling within the range which was explored in the present study.

Some experiments were carried out at different outlet pressures to investigate its effect upon the incident CHF. The results, plotted in Fig. 6 for different subcoolings, do not display any significant influence.

These experiments confirm the capability of such geometries to sustain an important incident heat flux of about 30 MW $m^{-2}$ in the subcooled boiling regime. The best result, within the explored range, corresponds to $\Phi_i = 46.7$ MW $m^{-2}$ for $D = 10$ mm; $L_H = 100$ mm; $G = 15.6$ Mg $m^{-2}$ $s^{-1}$; $T_{in} = 50°C$; $P_{out} = 3.6$ MPa. These experiments also show that the incident CHF is mainly sensitive to both mass flux and subcooling.

### 2.4. Determination of inner wall CHF from the incident CHF

For plasma facing components, only one side of the tube is heated by the incident flux that was experimentally determined in the present study. It may be reasonably expected that the dry-out responsible for the CHF occurrence will be directly related to the maximum flux at the inner wall for non symmetrical heating. Thus, it is necessary to determine the maximum CHF at the wall, $\Phi_c$, from the measured incident CHF, $\Phi_i$.

Let us define the peaking factor $F$ as the ratio between $\Phi_c$ and $\Phi_i$. As thermal resistance is mainly due to conduction within the solid, it may be anticipated from dimensional analysis that $F$ mainly depends on the fol-

Table 2
Experimental results

| Geometry | $L_H$ (mm) | $P_{out}$ (MPa) | $T_{in}$ (°C) | $T_{out}$ (°C) | $T_{sat}-T_{out}$ (°C) | $G$ (Mg m$^{-2}$ s$^{-1}$) | $\Phi_l$ (MW m$^{-2}$) | $\Phi_c$ (MW m$^{-2}$) | $F$ |
|---|---|---|---|---|---|---|---|---|---|
| 1 | 115 | 3.5 | 169 | 181 | 62 | 15 | 30.1 | 40.4 | 1.34 |
| | 105 | 3.5 | 172 | 182 | 61 | 14 | 27.0 | 35.9 | 1.33 |
| | 105 | 3.5 | 171 | 183 | 59 | 10 | 22.6 | 30.0 | 1.33 |
| | 105 | 3.4 | 171 | 188 | 53 | 5 | 15.3 | 20.3 | 1.33 |
| | 105 | 3.4 | 170 | 191 | 49 | 3 | 12.7 | 16.8 | 1.32 |
| 2 | 104 | 3.6 | 49 | 67 | 176 | 16 | 46.7 | 68.6 | 1.47 |
| | 100 | 3.6 | 50 | 68 | 176 | 15 | 44.7 | 65.7 | 1.47 |
| | 104 | 3.4 | 50 | 70 | 171 | 10 | 36.5 | 53.5 | 1.47 |
| | 104 | 3.6 | 97 | 110 | 133 | 15 | 34.2 | 49.9 | 1.46 |
| | 104 | 3.4 | 99 | 115 | 126 | 10 | 29.8 | 43.5 | 1.46 |
| | 104 | 3.6 | 146 | 156 | 87 | 15 | 26.0 | 37.8 | 1.45 |
| | 104 | 3.5 | 148 | 158 | 84 | 11 | 19.2 | 27.6 | 1.44 |
| | 100 | 3.2 | 165 | 174 | 63 | 16 | 23.8 | 34.5 | 1.45 |
| | 102 | 2.4 | 48 | 65 | 155 | 16 | 45.7 | 67.1 | 1.47 |
| | 102 | 2.3 | 49 | 66 | 152 | 14 | 42.6 | 62.5 | 1.47 |
| | 102 | 2.5 | 96 | 108 | 114 | 16 | 31.0 | 44.9 | 1.45 |
| | 102 | 2.7 | 147 | 156 | 71 | 15 | 22.8 | 32.9 | 1.44 |
| | 104 | 1.3 | 49 | 64 | 125 | 14 | 37.3 | 54.7 | 1.47 |
| | 104 | 1.2 | 50 | 67 | 117 | 10 | 29.5 | 42.9 | 1.45 |
| | 104 | 1.0 | 50 | 75 | 104 | 5 | 21.0 | 30.6 | 1.46 |
| 3 | 85 | 3.4 | 35 | 49 | 192 | 6 | 30.4 | 39.2 | 1.29 |
| | 102 | 3.6 | 49 | 59 | 184 | 13 | 39.8 | 52.0 | 1.31 |
| | 102 | 3.4 | 49 | 59 | 182 | 10 | 31.6 | 40.0 | 1.27 |
| | 92 | 3.3 | 60 | 71 | 168 | 9 | 29.3 | 37.2 | 1.27 |
| | 85 | 3.4 | 59 | 74 | 167 | 6 | 28.4 | 36.1 | 1.27 |
| | 102 | 3.7 | 97 | 106 | 139 | 12 | 33.3 | 42.1 | 1.26 |
| | 102 | 3.5 | 98 | 107 | 134 | 10 | 27.8 | 35.1 | 1.26 |
| | 96 | 3.3 | 100 | 110 | 128 | 9 | 30.3 | 38.4 | 1.27 |
| | 85 | 3.4 | 99 | 113 | 128 | 5 | 26.3 | 33.5 | 1.27 |
| | 102 | 3.6 | 146 | 153 | 91 | 12 | 24.9 | 31.5 | 1.27 |
| | 102 | 3.6 | 146 | 154 | 90 | 10 | 25.2 | 31.9 | 1.27 |
| | 85 | 3.6 | 149 | 157 | 87 | 8 | 24.2 | 30.8 | 1.27 |
| | 85 | 3.4 | 149 | 161 | 80 | 5 | 21.5 | 27.4 | 1.27 |
| | 102 | 2.4 | 49 | 59 | 160 | 12 | 37.8 | 48.1 | 1.27 |
| | 102 | 2.3 | 49 | 59 | 158 | 10 | 31.0 | 39.4 | 1.27 |
| | 102 | 2.4 | 97 | 105 | 116 | 12 | 32.7 | 41.5 | 1.27 |
| | 102 | 2.4 | 98 | 107 | 113 | 10 | 26.8 | 33.9 | 1.26 |
| | 85 | 2.3 | 99 | 108 | 110 | 9 | 27.2 | 34.5 | 1.27 |
| | 102 | 1.4 | 49 | 57 | 136 | 13 | 32.6 | 41.4 | 1.27 |
| | 96 | 1.3 | 60 | 70 | 119 | 9 | 29.3 | 37.2 | 1.27 |
| | 85 | 1.4 | 59 | 71 | 122 | 5 | 22.7 | 28.8 | 1.27 |
| | 85 | 1.4 | 99 | 106 | 86 | 9 | 25.4 | 32.2 | 1.27 |
| | 85 | 1.4 | 99 | 109 | 84 | 5 | 19.2 | 24.3 | 1.27 |
| 4 | 100 | 3.2 | 49 | 58 | 179 | 9 | 35.8 | 45.3 | 1.27 |
| | 100 | 3.2 | 49 | 58 | 180 | 8 | 28.1 | 36.0 | 1.28 |
| | 100 | 3.3 | 97 | 105 | 134 | 8 | 23.5 | 29.3 | 1.25 |
| | 100 | 3.2 | 146 | 152 | 85 | 7 | 19.3 | 24.0 | 1.24 |

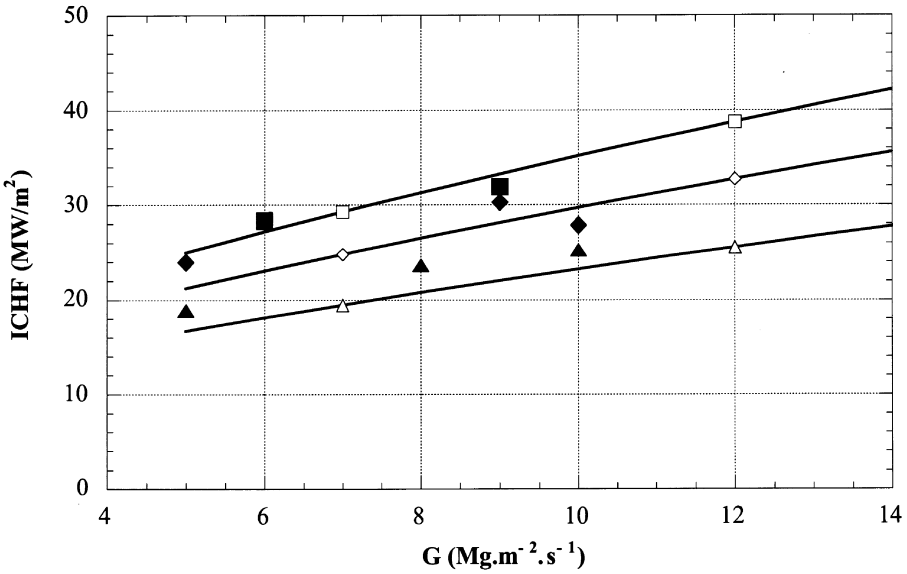


Fig. 4. Incident CHF vs. mass flux for different outlet subcoolings and for $P_{out} = 3.5$ MPa, $D = 14$ mm, $w = 19$ mm, $L_H = 100$ mm and $\Delta T_{sub,out} = 80°C$ (test: ▲, calculation: —△—), 120°C (test: ◆, calculation: —◇—), 170°C (test: ■, calculation: —□—).

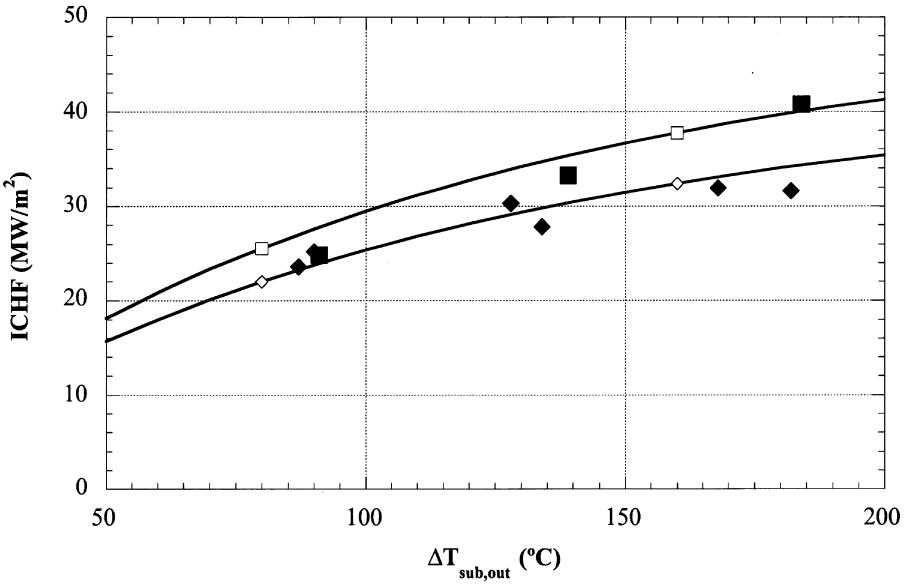


Fig. 5. Incident CHF vs. outlet subcooling for different mass fluxes and for $P_{out} = 3.5$ MPa, $D = 14$ mm, $w = 19$ mm, $L_H = 100$ mm and $G = 10$ Mg m$^{-2}$ s$^{-1}$ (test: ◆, calculation: —◇—), 12 Mg m$^{-2}$ s$^{-1}$ (test: ■, calculation: —□—).

lowing geometrical parameters of the test section: $w/D$, $t/D$. The relation between $F$ and the foregoing parameters is a priori unknown. However, it may be determined by solving the heat conduction in the solid, provided that boundary conditions at the inner wall are known. This was numerically obtained by a finite element method, using convective and subcooled boiling heat transfer correlations as boundary conditions [17]. Figure 7 gives an illustration of this calculation. The temperature of onset of nucleate boiling (ONB) [18] shows the limit between the heat transfer regimes. Subcooled boiling regime occurs at the upper part of the wall whereas convective regimes occurs at the lower part. It exhibits at the wall a non homogeneous distribution of both temperature and

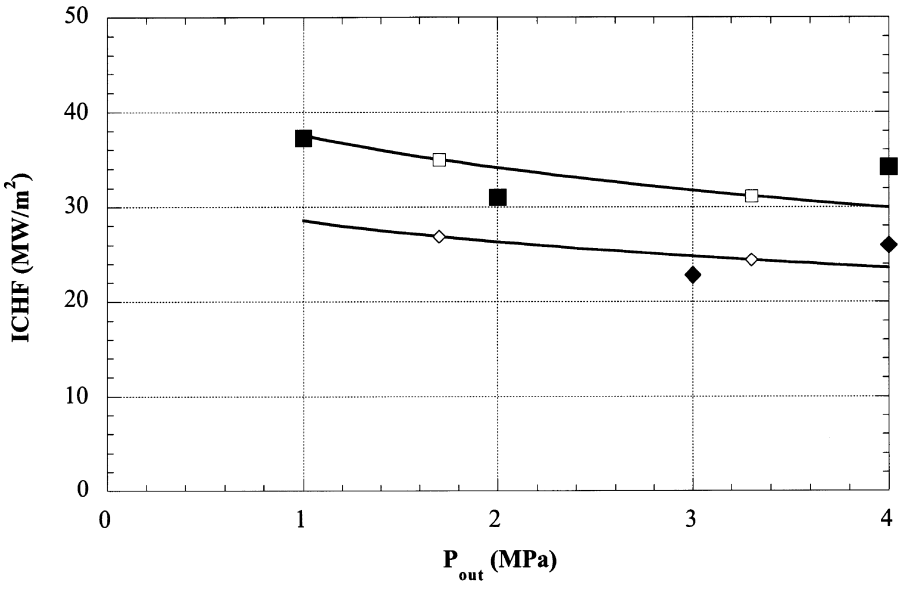


Fig. 6. Incident CHF vs. outlet pressure for different outlet subcooling and for $G = 15$ Mg m$^{-2}$ s$^{-1}$, $D = 10$ mm, $w = 17$ mm, $L_H = 100$ mm and $\Delta T_{sub,out} = 120$°C (test: ◆, calculation: —◇—), 170°C (test: ■, calculation: —□—).

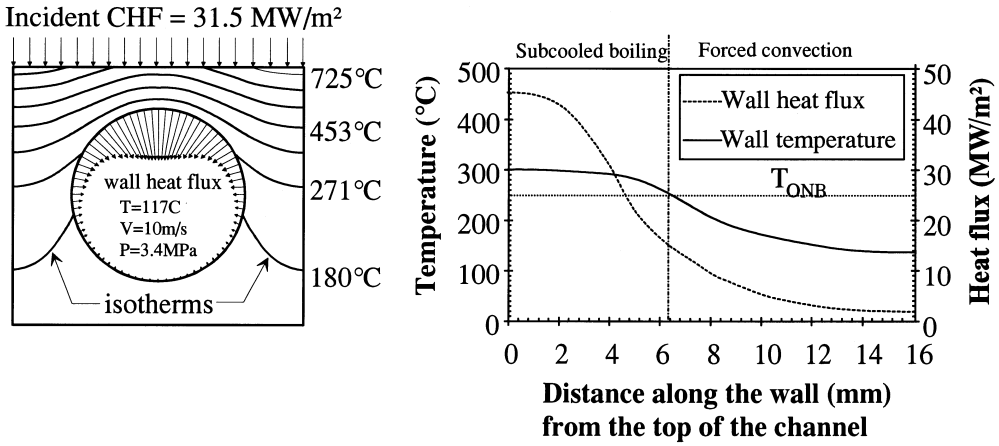


Fig. 7. Heat flux and temperature distribution at the inner wall for $P_{out} = 3.4$ MPa, $T_{out} = 115$°C, $G = 11$ Mg m$^{-2}$ s$^{-1}$, $D = 10$ mm, $w = 17$ mm, $L_H = 100$ mm.

heat flux. The peaking factor was calculated for the following range of the geometrical parameters: $1.33 \leqslant w/D \leqslant 1.7$, $0.08 \leqslant t/D \leqslant 0.3$. It may be expressed within 10% of accuracy by the correlation:

$$F = \left(\frac{w}{D}\right)\left[1 - \frac{1}{6}\left(\frac{w}{D}\right)^{-2}\right]\left[1 - \left(\frac{t}{D}\right)^{4}\right] \quad (2)$$

## 3. Modelling

The CHF mechanism in subcooled flow is not yet completely understood in spite of various experimental studies. Different models exist: they are classified according to the basic mechanism assumed to be the cause of CHF [19–22]. Among them, the model of Celata et al. [14, 15] is the first dedicated to fusion reactors. It was developed over a wide range of thermal hydraulic conditions for vertical upflow in uniformly heated tubes. It is generally acknowledged that this model has a good predictive capability although it is complex to use.

We shall demonstrate, in the first part of this section, that the Celata et al. model can be considerably simplified without any significant loss of accuracy. The correlation deduced from this simplification will be compared to

the model for uniform heating in vertical tubes. Then, a modification of the correlation for plasma facing components will be discussed.

### 3.1. CHF mechanism as proposed by Celata et al.

According to Celata et al., CHF occurs when the superheated liquid layer disappears at the wall leading to dry-out. This concept, first introduced by Lee and Mudawar [23], was further used by Lin et al. [24] and improved by Katto [25, 26]. During subcooled boiling, small bubbles rise along the near wall region. Their coalescence results in the formation of 'vapour blankets' located within the superheated layer in the vicinity of the heated wall as shown in Fig. 8. These vapour blankets appear as vertical elongated and distorted bubbles whose thickness $D_b$ is almost equal to the diameter of a bubble at departure from the heated wall. These blankets overlie a very thin liquid sublayer in contact with the wall. Celata et al. assumed that the dry-out at the wall occurs when the length of the vapour blanket reaches the critical wavelength of Kelvin–Helmholtz instability at the liquid–vapour interface.

The thickness $\delta_b$ of the liquid sublayer is equal to $y_{sat}-D_b$, where $y_{sat}$ is the superheated layer thickness. The vapour blanket is characterised by its length $L_b$ and its velocity $U_b$. According to the model, if the sublayer velocity is negligible with respect to the blanket velocity, the CHF $\Phi_c$ is given by:

$$\frac{\Phi_c}{\rho_L U_b i_{fg}} = \frac{\delta_b}{L_b} \tag{3}$$

where $\rho_L$ is the liquid density and $i_{fg}$ the latent heat of vaporization. Where not specified, physical properties are calculated at saturated state corresponding to $P_{out}$. CHF conditions are then calculated with an iterative method introducing closure laws for the different parameters involved in equation (3), $y_{sat}$ and the characteristics of the vapour blanket $L_b$, $D_b$, $U_b$. With the view to suppress the iterative procedure, we will discuss these laws and simplify their expression whenever possible.

### 3.2. CHF modelling for parallel flow in uniformly heated tube

Let us restrict our attention to the case of vertical nonswirling upflow in uniformly heated tubes.

#### 3.2.1. Vapour blanket velocity

In their model, Celata et al. adopted the assumption of Lee and Mudawar to predict the velocity of the vapour blanket. They supposed that this velocity is the sum of the velocity that the liquid would have in single phase flow at the centre of the blanket and the slip velocity of the blanket determined from a force balance.

The velocity of the liquid is determined from classical near wall distributions valid for viscous sublayer, matching layer or inertial layer. Because of the high values of the Reynolds number in CHF situations, the viscous sublayer is so thin that the vapour blanket is located within the inertial sublayer. In this layer the velocity does not vary significantly with the distance from the wall so that it may be assumed equal to the bulk velocity $U_L$. Replacing the local velocity by the bulk velocity does not lead to significant differences. Therefore, this simplification was introduced in our model.

The force balance used to predict the slip velocity of

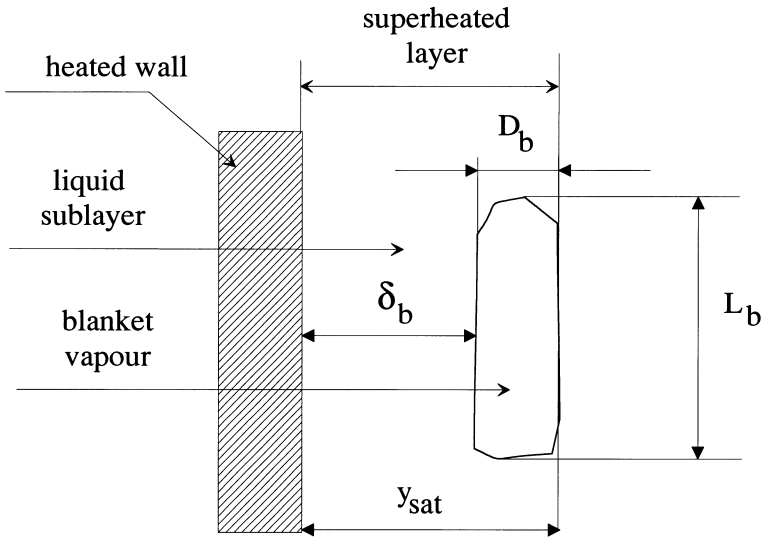


Fig. 8. CHF mechanism according to Celata et al.

the blanket involves buoyancy and drag. On the one hand, the expression of the drag force which was used by Celata et al. is highly questionable for bubbles of such small size. On the other hand, the numerical simulations realized for the present thermal hydraulic conditions [27] proved that this velocity is always very small and can be neglected. The blanket velocity has thus been considered to move at the bulk velocity of the liquid:

$$U_b = U_L. \tag{4}$$

*3.2.2. Length of vapour blanket*

The blanket length $L_b$ is supposed to be equal to the critical wavelength of the liquid–vapour interface, determined from the Kelvin–Helmholtz instability theory. Introducing equation (4) in the expression proposed by Lee and Mudawar, $L_b$ is now determined from input physical quantities instead of using the complex procedure of Celata et al. that involves an iterative process:

$$L_b = \frac{2\pi\sigma(\rho_V+\rho_L)}{\rho_V\rho_L U_L^2} \tag{5}$$

where $\rho_V$ is the vapour density and $\sigma$ the surface tension.

*3.2.3. Diameter of vapour blanket*

The vapour blanket is formed with bubbles that rise and coalesce near the heated wall. Its thickness $D_b$ corresponds to the diameter of these bubbles when they depart from the wall. As proposed by Staub [28], their diameter may be expressed as

$$D_b = \frac{0.24}{f}\frac{\sigma\rho_L}{G^2} \tag{6}$$

where $f$ is the wall friction factor.

*3.2.4. Friction factor*

$f$ is calculated using the Colebrook–White correlation. CHF approaching, the wall friction is assumed to be controlled by the hydrodynamic roughness due to the bubbles growing at the wall (Levy [29]). It is given by

$$\frac{1}{\sqrt{f}} = 2.28 - 4\log\left(\frac{0.75D_b}{D} + \frac{4.675}{Re\sqrt{f}}\right), \tag{7}$$

where $Re = U_L D/\nu_L$ is the Reynolds number.

The first term within the parentheses corresponds to the contribution of roughness whereas the second term corresponds to the contribution of viscous effect. Numerical simulations revealed the predominance of the roughness for the CHF situations. Therefore, the friction factor correlation was simplified to yield:

$$\frac{1}{\sqrt{f}} = 2.28 - 4\log\left(\frac{0.75D_b}{D}\right). \tag{8}$$

*3.2.5. Temperature distribution*

CHF prediction from equation (3) requires the determination of the thickness of the superheated liquid layer and thus of $y_{sat}$ knowing the near wall temperature profile. In spite of the presence of the vapour blanket, Celata et al. used the single-phase flow correlations proposed by Martinelli [30] for predicting the near wall temperature. These correlations predict the temperature within the viscous sublayer, the matching layer and the inertial layer. Using this model, numerical simulations have shown that the vapour blanket is always located in the inertial layer. Kader and Yaglom [31] proposed a simpler model valid in this region ($y^+ \geqslant 30$):

$$T^+ = \frac{Pr_t}{\kappa}\ln y^+ + C_0 \tag{9}$$

where $\kappa$ is the von Karman constant equal to 0.4 and $C_0$ another constant that depends on the turbulent Prandtl number $Pr_t$ ($\approx 0.85$) and on the physical properties of the liquid through the Prandtl number $Pr$:

$$C_0 = \frac{Pr_t}{\kappa}\ln Pr + 12.5Pr^{2/3} - 5.3. \tag{10}$$

In the above expression the dimensionless temperature $T^+ = (T_w - T)/\theta_*$ is scaled by the friction temperature defined as:

$$\theta_* = \frac{\Phi}{\rho_L C_p u_*}. \tag{11}$$

The dimensionless distance $y^+ = yu_*/\nu_L$ is expressed vs. the friction velocity:

$$u_* = U_L\sqrt{\frac{f}{2}}. \tag{12}$$

This model is in close agreement with the Martinelli model in the inertial layer. In view of its simplicity it has been used in the present study.

*3.2.6. Superheated layer thickness*

$y_{sat}$ is calculated from the integration of the temperature profile along the radius of the channel. Like in the model of Celata et al., due to high Reynolds number in CHF situation, the thermal layer is very thin and the temperature profile can only be integrated in the inertial layer. Kader and Yaglom [31] proposed a model valid in this region:

$$\frac{1}{St} = \sqrt{\frac{2}{f}}(C_0 + C_1) \tag{13}$$

where $St = \Phi_w/[GC_P(T_w - T_{out})]$ is the Stanton number. $\Phi$ is the wall heat flux, $T_w$ the wall temperature, $T_{out}$ the water outlet temperature and $C_P$ is the specific heat at constant pressure. $C_1$ is a constant that depends on the turbulent Prandtl number, the von Karman constant, the Reynolds number and the friction factor:

$$C_1 = \frac{Pr_t}{\kappa}\left[\ln(Re\sqrt{f}) + \frac{5}{4\kappa}\sqrt{\frac{f}{2}} - \frac{3}{2} - \frac{\ln 2}{2}\right]. \tag{14}$$

Introducing the Stanton number, equation (13) becomes

$$\frac{T_w - T_{out}}{T_*} = C_0 + C_1. \quad (15)$$

$T_w$ is unknown and can be eliminated combining equations (9) and (15):

$$\frac{T_{out} - T}{T_*} = \frac{Pr_t}{\kappa} \ln\left(\frac{yu_*}{\nu_L}\right) - C_1. \quad (16)$$

This relation expresses the fluid temperature, $T$, as a function of the distance from the heated wall, $y$. Consequently, the distance $y_{sat}$ from the heated wall at which the fluid temperature is equal to the saturation temperature is given by:

$$\frac{y_{sat}u_*}{\nu_L} = \exp\left\{\frac{\kappa}{Pr_t}\left[\left(\frac{\rho_L C_P u_*(T_{out} - T_{sat})}{\Phi_w}\right) + C_1\right]\right\}. \quad (17)$$

The outlet temperature is calculated from the energy balance

$$Y_{out} = T_{in} + \frac{\Phi_i S_H}{GSC_{P,in}} \quad (18)$$

where $S_H = \pi D L_H$ is the heat transfer surface, $S$ the section of passage of the fluid. For uniformly heated tube, the incident heat flux $\Phi_1$ is equal to the wall heat flux $\Phi_w$, provided that the thickness of the tube is thin enough compared to the diameter. Introducing equation (18) in equation (17), $y_{sat}$ can be expressed as

$$\frac{y_{sat}u_*}{\nu_L} = \exp\left\{\frac{\kappa}{Pr_t}\sqrt{\frac{f}{2}}\left[\frac{x_{in}}{Bo} + C_2\frac{S_H}{S} + \sqrt{\frac{2}{f}}C_1\right]\right\} \quad (19)$$

where $x_{in} = [C_P(T_{in} - T_{sat})]/i_{fg}$ is the inlet enthalpic mass quality, $Bo_w = \Phi_w/(\rho_L U_L i_{fg})$ is the boiling number and $C_2 = (\rho_L/\rho_{L,in})(C_P/C_{P,in})$.

### 3.2.7. Critical heat flux

The final CHF expression is calculated introducing the expression for $y_{sat}$ given by equation (19) in the CHF definition [equation (3)]:

$$\frac{x_{in}}{Bo_c} = \frac{Pr_t}{\kappa}\sqrt{\frac{2}{f}} ln\left[\sqrt{\frac{2}{f}}\frac{U_L L_b}{\nu_L}\left(Bo_c + \frac{D_b}{L_b}\right)\right] - C_2\frac{S_H}{S} - \sqrt{\frac{2}{f}}C_1 \quad (20)$$

where $Bo_c$ corresponds to CHF, $\Phi_c$.

Numerical simulations over the database of Celata et al. showed that

$$Bo_c \ll D_b/L_b. \quad (21)$$

Thanks to this simplification, equation (20) becomes an explicit function of the boiling number and CHF can be calculated from

$$Bo_c = \frac{x_{in}}{\frac{Pr_t}{\kappa}\sqrt{\frac{2}{f}}\ln\left[\frac{C_3}{\sqrt{f}}\frac{Re}{We}\right] - C_2\frac{S_H}{S} - \sqrt{\frac{2}{f}}C_1} \quad (22)$$

where $We = \rho_L U_L^2 D/\sigma$ is the Weber number and $C_3 = (0.24/\sqrt{2})(\rho_L/\rho_{L,in})^2\sqrt{1/f}$.

These above simplifications allow an explicit calculation of CHF. This new expression was evaluated from the Celata database within the range: $25 \leqslant \Delta T_{sub,in} \leqslant 255$ K; $1 \leqslant P \leqslant 8.4$ MPa; $0.3 \leqslant D \leqslant 25.4$ mm; $2.5 \leqslant L_H \leqslant 610$ mm; $0.9 \leqslant G \leqslant 90\,000$ kg m$^{-2}$ s$^{-1}$; $3.3 \leqslant \Phi_v \leqslant 227.9$ MW m$^{-2}$. Figure 9 shows a good agreement between experiment and calculation, using equation (22): about 90% of predicted points within $\pm 30\%$ range.

## 3.3. CHF modelling for parallel flow in one-side heated tube

Let us introduce the specific conditions of plasma facing components in this new relation.

### 3.3.1. Heat balance

As already mentioned, the one-side heating condition leads to distinguish the incident CHF, $\Phi_1$, from the maximum wall heat flux $\Phi_c$. A relation has been established between these two heat fluxes by introducing the peaking factor $F$ in equation (2). Thus the heat balance equation can be expressed as a function of $\Phi_c$:

$$T_{out} = T_{in} + \frac{\Phi_c}{F}\frac{S_{H1}}{GSC_{P,in}} \quad (23)$$

where $S_{H1} = w_H L_H$ is the heated section (see Fig. 1).

### 3.3.2. Temperature scale

As shown in Fig. 7, the distribution of the temperature at the wall is non-uniform due to the fact that only one side is heated. To take into account this effect, the dimensionless temperature $T^+$ is scaled by the average friction temperature $\bar{\theta}_*$ defined as a function of the average heat flux at the wall, $\bar{\Phi}_c$:

$$\bar{\theta}_* = \frac{\bar{\Phi}_c}{\rho_L C_P u_*}. \quad (24)$$

$\bar{\Phi}_c$ is characteristic of CHF occurrence at the wall. When CHF occurs, numerical calculations showed that the wall circumference where boiling occurs was about 38% of the inner perimeter, whatever the thermal hydraulic conditions i.e. temperature, pression and mass flux. Thus, it is shown that the limit of the thermal performance is controlled by the geometry. The transfer of heat to the cooling liquid is limited by a maximum wall heat flux value but also by the maximum wall area over which it applies. These two phenomena are expected to be coupled and numerical calculations showed that a constant ratio $C_4$ between $\bar{\Phi}_c$ and $\Phi_c$ exists:

$$\bar{\Phi}_c = C_4\Phi_c \quad C_4 = 2/3. \quad (25)$$

Within our experimental range, the pure effect of the geometry, is also pointed out by the expression of the

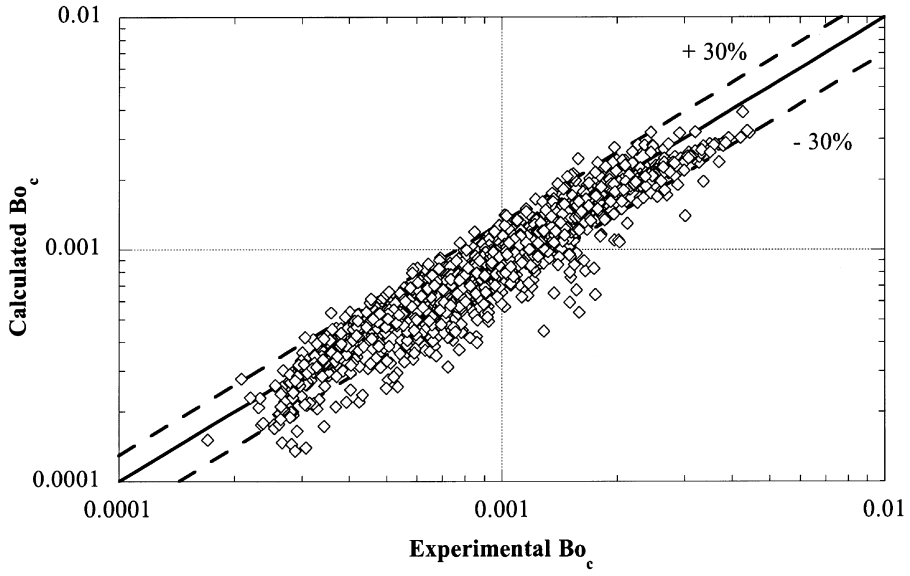


Fig. 9. Calculated vs. experimental boiling number using the Celata et al. database.

peaking factor, that depends only on the geometrical parameters of the test section.

### 3.3.3. Critical heat flux

The final relation for one-side heated tube cooled by a parallel flow is deduced by introducing the above equations (23)–(25) in equation (22):

$$Bo_c = \frac{x_{in}/C_4}{\frac{Pr_t}{\kappa}\sqrt{\frac{2}{f}}\ln\left[\frac{C_3}{\sqrt{f}}\frac{Re}{We}\right] - \frac{1}{F}\frac{C_2}{C_4}\frac{S_{H1}}{S} - \sqrt{\frac{2}{f}}C_1} \quad (26)$$

The comparison of this correlation with experimental results in terms of boiling numbers is presented in Fig. 10 within the range: $D = 10$ mm, $w = 15$ mm, $t = 1.5$ mm, $P_{out} = 3.5$ MPa; $0.05 \leqslant L_H \leqslant 0.15$ m; $4.8 \leqslant G \leqslant 14.4$ Mg m$^{-2}$ s$^{-1}$; $95 \leqslant \Delta T_{sub,in} \leqslant 195$°C. A good agreement between experiment and calculation is observed within a $\pm 20\%$ range.

## 3.4. One-side heated tube, swirl flow

With respect to the previous conditions, the channel is equipped with a twisted-tape acting as a turbulence promoter that creates an helicoidal movement of the water flow.

### 3.4.1. Friction factor

The presence of the tape in the channel increases the wetted perimeter. The friction factor depends on the equivalent hydraulic diameter $Dh_{sw}$ expressed as the ratio between the section of passage of the fluid and the wetted perimeter:

$$Dh_{sw} = 4S_{sw}/(\pi D + 2D - 2t_{sw}) \quad (27)$$

where $S_{sw} = (\pi D^2/4) - Dt_{sw}$ is the section passage of the fluid. However, friction is mainly controlled by the rough part of the tube over which bubbles are produced.

The friction factor is given by [see equation (8)]

$$\frac{1}{\sqrt{f_{sw}}} = 2.28 - 4\log\left(\frac{0.75D_b}{Dh_{sw}}\right) \quad (28)$$

### 3.4.2. Reynolds number

The twisted-tape modifies the flow of the fluid and enhances the turbulence. The Reynolds number, $Re_{sw}$, is defined as

$$Re_{sw} = U_{sw}Dh_{sw}/v_L \quad (29)$$

where $U_{sw} = U_L\sqrt{1+(\pi/2\omega)^2}$ is the swirl velocity $U_{sw}$ [32].

$Re_{sw}$ is introduced in the constant $C_1$ [see equation (14)], which becomes $C_{1,sw}$.

### 3.4.3. Critical heat flux

The final relation for a tube heated on one side and cooled by a swirling flow is deduced by introducing the above equations (28) and (29) in equation (22):

$$Bo_c = C_5\frac{x_{in}/C_4}{\frac{Pr_t}{\kappa}\sqrt{\frac{2}{f_{sw}}}\ln\left[\frac{C_3}{\sqrt{f_{sw}}}\frac{Re}{We}\right] - \frac{1}{F}\frac{C_2}{C_4}\frac{S_{H1}}{S_{sw}} - \sqrt{\frac{2}{f_{sw}}}C_{1,sw}} \quad (30)$$

where $C_5 = 1.7e^{x}{}_{in}$ is an empirical coefficient, function of the inlet mass quality. As pointed out by Celata et al., a systematic error was detected when the outlet tem-

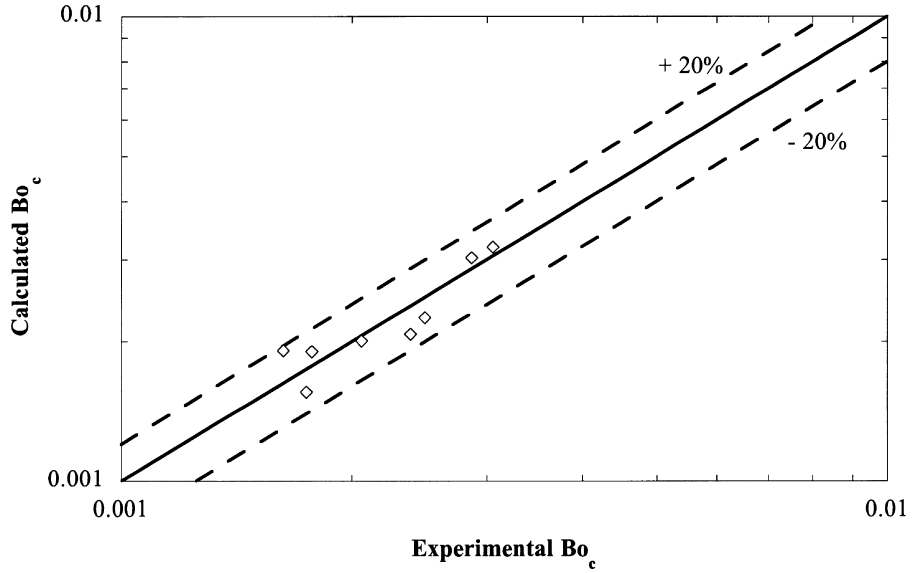


Fig. 10. Calculated vs. experimental boiling number for one-side heating conditions, parallel flow.

perature was approaching the saturation temperature. The role of this coefficient is to reduce this effect. The comparison between calculation and experiment is illustrated in Fig. 11 within the ranges: $10 \leqslant D \leqslant 18$ mm, $15 \leqslant w \leqslant 24$, $1.5 \leqslant t \leqslant 2.4$ mm, $1 \leqslant P_{out} \leqslant 3.7$ MPa; $L_H = 0.1$ m; $3 \leqslant G \leqslant 16$ Mg m$^{-2}$ s$^{-1}$; $70 \leqslant \Delta T_{sub,in} \leqslant 195$°C. The model predicts with a reasonable accuracy the experimental data within a $\pm 20\%$ range. The evolution of the correlation versus the thermal hydraulic parameters is presented in Figs 4–6. The incident CHF is calculated using the correlation of the peaking factor given in equation (2). The comparison demonstrates that the correlation is reasonably accurate in predicting CHF tendencies versus mass flux, outlet subcooling and pressure.

### 3.5. Effect of inserted twisted tape on CHF

The influence of the twisted tape on CHF under one-side heating conditions is evaluated by comparing the

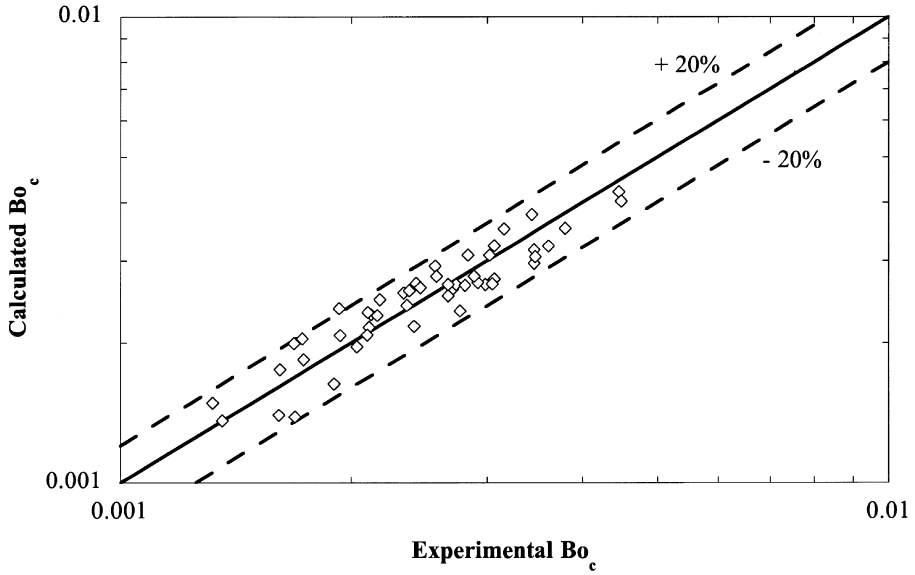


Fig. 11. Calculated vs. experimental boiling number for one-side heating conditions, swirl flow.

predictions of equation (26) for parallel flow and equation (30) for swirl flow (Fig. 12). For the same hydraulic conditions, the twisted tape increases the wall CHF by about 40% in average. However this effect decreases as the outlet subcooling increases. Since this tape is thin, the improvement of CHF mainly results from the swirl. As shown by the prediction of Fig. 12, a twist ratio of two is acceptable. However, it is difficult to determine the respective influence of both twist ratio and tape thickness on CHF since only one geometry was tested.

## 4. Conclusion

This paper provides new correlations for predicting CHF under thermal hydraulic operating conditions of plasma facing components.

The experiments performed in an electron beam gun facility proves the thermal hydraulic ability of one-side heated swirl tubes cooled in the subcooled regime to remove high heat fluxes in the range of 30 MW $m^{-2}$. It is shown that the main parameters capable of providing a significant CHF enhancement are the mass flux and the subcooling.

The incident heat flux, which was experimentally determined, does not control directly CHF at the inner wall. To characterize one-side heating conditions, a peaking factor was introduced to establish a relation between the incident CHF an the wall CHF, defined as the maximum heat flux at the wall. This maximum heat flux at critical condition is predicted from a correlation deduced from the liquid sublayer dryout mechanism model proposed by Celata et al. The first step consisted in the significant simplification of this model for the case of uniform heated tube cooled by a parallel flow. This simplified model led to a reasonable accuracy for the database of Celata et al. The model was then adopted to the specific cases of one-side heated tubes cooled by a parallel or a swirling subcooled flow. In both cases, experiments were predicted by this new correlation with an accuracy better than 20%.

## Acknowledgements

The authors wish to thank the NET team and the CEA Cadarache for their financial support. They are also indebted to the FE 200 team of Framatome for carrying out these tests.

## References

[1] J.B. Whitley, J.A. Koski, R. Aymar, Engineering considerations for the Tore Supra pump limiter, Proc. 14eme Symp. Fusion Technol., Avignon, France, 1986.
[2] Tore Supra Team, Towards long pulse high performance discharges in Tore Supra: Experimental knowledge and technological developments for heat exhaust, Fusion Technol. 29 (4) (1996) 417–448.

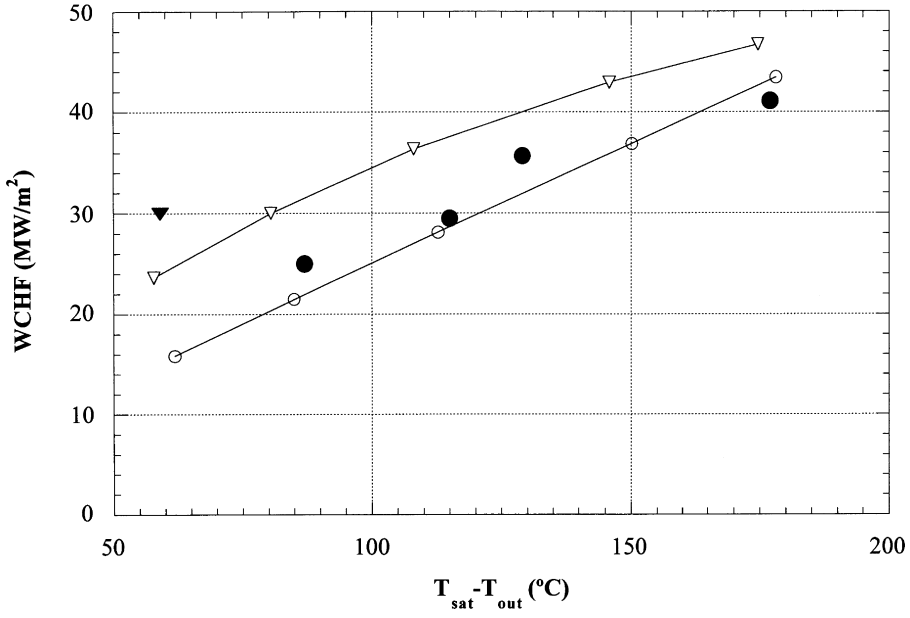


Fig. 12. Wall CHF vs. outlet subcooling for smooth (test: ●, calculation: —○—) and swirl ($\omega = 2$, $t_{sw} = 0.8$ mm) tube (test: ▼, calculation: —▽—) and for $P_{out} = 3.5$ MPa, $G = 10$ Mg $m^{-2}$ $s^{-1}$, $D = 10$ mm, $w = 15$ mm, $L_H = 100$ mm.

[3] P.H. Rebut, ITER: The first experimental fusion reactor, Fusion Engng Design 30 (1995) 85–118.
[4] J.G. Collier, J.R. Thorne, Convective Boiling and Condensation, 3rd edn. Oxford University Press, 1994.
[5] R.D. Boyd, Subcooled flow boiling critical heat flux (CHF) and its application to fusion energy components. Part I: a review of fundamentals of CHF and related database, Fusion Technol. 7 (1985) 7–29.
[6] L.S. Tong, A phenomenological study of critical heat flux, ASME paper, 75-HT-68, 1975.
[7] J.A. Koski, A.G. Beattie, J.B. Whitley, C.D. Croessman, Experimental verification of subcooled flow boiling for Tokamak pump limiter designs, National Heat Transfer Conference, ASME 87-HT-45, Pittsburgh, 1987.
[8] S.T. Yin, A thermalhydraulics package for NET divertor heat transfer and pressure drop analysis, Specialists' Workshop on Divertor Plate Thermalhydraulics. San Francisco, 1991.
[9] J. Schlosser, A. Cardella, P. Massman, P. Chappuis, H.D. Falter, P. Deschamps, G.P. Deschamps, thermal-hydraulic tests on NET divertor targets using swirl tubes, 7th Proc. Nuclear Thermal Hydraulics ANS Winter Meeting (1991) 26–31.
[10] M. Akiba, R.D. Watson, Thermo-hydrodynamic coupling with coolants, in: R.K. Janev, H.W. Darwin (Eds.), in: Atomic and Plasma-Material Interaction Processes in Controlled Thermonuclear Fusion, Elsevier Science Publishers B.V., New York, 1993, pp. 455–480.
[11] V. Divavin, V. Tanchuk, A. Shrubok, R. Watson, J. Gonzales, An experimental and numerical investigation of post-CHF heat transfer for one-sided heat load with highly subcooled flow boiling, Fusion Engng Design 31 (1996) 189–200.
[12] J. Schlosser, J. Boscary, F. Escourbiac, I. Smid, G. Vieider, comparison between various thermal hydraulic tube concepts for the ITER divertor, Proc. 19th Symp. Fusion Technol., Lisbon, Portugal (1996), pp. 263–266.
[13] M. Araki, K. Sato, S. Suzuki, M. Akiba, Critical heat flux experiment on the screw tube under one-side heating conditions, Fusion Technol. 29 (1996) 519–528.
[14] G.P. Celata, M. Cumo, A. Mariani, M. Simoncini, G. Zumo, Rationalization of existing mechanistic models for the prediction of water subcooled flow boiling critical heat flux, Int. J. Heat Mass Transfer 37 (1) (1994) 347–360.
[15] G.P. Celata, M. Cumo, A. Mariani and G. Zumo, The prediction of the critical heat flux in water-subcooled flow boiling, Int. J. Heat Mass Transfer 38 (6) (1995) 1111–1119.
[16] G. Mayaux, A. Cardella, P. Chappuis, P. Deschamps, M. Febvre, J.Y. Journeauz, H. Viallet, 200 kW electron gun facility for plasma facing component tests, Fusion Technol. 1 (1992) 317–321.
[17] J. Schlosser, J. Boscary, Thermal-hydraulic tests at NET/ITER relevant conditions on divertor targets using swirl tubes, Proc. NURETH 6, 815–824, Grenoble, France, 1993.
[18] A.E. Bergles, W.M. Rohsenow, The determination of forced-convection surface boiling heat transfer, J. Heat Transfer (1964) 365–372.
[19] L.S. Tong, G.F. Hewitt, Overall viewpoint of flow boiling CHF mechanisms, ASME 72-HT-54, 1972.
[20] A.E. Bergles, Burnout in boiling heat transfer. Part II: subcooled and low quality forced-convection systems, Nuclear Safety 18 (2) (1977) 154–167.
[21] G.F. Hewitt, Critical heat flux in flow boiling, Proc. Sixth Int. Heat Transfer Conf. (1978) 143–171.
[22] Y. Katto, Critical heat flux, Int. J. Multiphase Flow 20 (1994) 53–90.
[23] C.H. Lee, I. Mudawar, A mechanistic critical heat flux model for subcooled flow boiling based on local bulk flow conditions, Int. J. Multiphase Flow 14 (1988) 711–728.
[24] W.S. Lin, C.H. Lee, B.S. Pei, An improved theoretical critical heat flux model for low quality flow, Nuclear Technology 88 (1989) 294–306.
[25] Y. Katto, Prediction of critical heat flux of subcooled flow boiling in round tubes. Int. J. Heat Mass Transfer 33 (1990) 1921–1928.
[26] Y. Katto, A prediction model of subcooled water flow boiling CHF for pressure in the range 0.1–20 MPa, Int. J. Heat Mass Transfer 35 (1992) 1115–1123.
[27] J. Boscary, Transfert thermique et flux critique dans un écoulement hélicoïdal en tube chauffé non uniformément, Ph.D. thesis, Institut National Polytechnique de Toulouse, France, 1995.
[28] F.W. Staub, The void fraction in subcooled boiling-prediction of the initial point of net vapour generation, J. Heat Transfer 90 (1968) 151–157.
[29] S. Levy, Forced convection subcooled boiling—prediction of vapour volumetric fraction, Int. J. Mass Transfer 10 (1967) 951–965.
[30] R.C. Martinelli, Heat transfer to molten metals, ASME Trans. 69 (1947) 947–959.
[31] B.A. Kader, A.M. Yaglom, Heat and mass transfer laws for fully turbulent wall flows, Int. J. Mass Transfer 15 (1972) 2329–2351.
[32] R.F. Lopina, A.E. Bergles, Heat transfer and pressure drop in tape generated swirl flow, J. Heat Transfer 91 (1969) 434–442.